

Investigations of Temporal and Spatial Distribution of Precursors SO₂ and NO₂ Vertical Columns in North China Plain by Mobile DOAS

Fengcheng Wu¹, Pinhua Xie^{1,3,4*}, Ang Li¹, Fusheng Mou¹, Hao Chen¹, Yi Zhu², Tong
5 Zhu², Jianguo Liu¹, Wenqing Liu¹

[1] Key Laboratory of Environmental Optical and Technology, Anhui Institute of Optics and Fine Mechanics, Chinese Academy of Sciences, Hefei, 230031, China

[2] State Key Laboratory of Environmental Simulation and Pollution Control, College of Environmental Sciences and Engineering, Peking University, Beijing, 100871,
10 China

[3] Center for Excellence in Regional Atmospheric Environment, Institute of Urban Environment, Chinese Academy of Sciences, Xiamen, 361021, China

[4] School of Environmental Science and Optoelectronic Technology, University of Science and Technology of China, Hefei, 230026, China

15 *Correspondence to:* P. H. Xie (phxie@aiofm.ac.cn)

Abstract: Recently, Chinese cities have suffered severe events of haze air pollution, particularly in North China Plain (NCP). Investigating the temporal and spatial distribution of pollutants, emissions, and pollution transport is necessary to better understand the effect of various sources on air quality. We
20 report on mobile differential optical absorption spectroscopy (mobile DOAS) observations of precursors SO₂ and NO₂ vertical columns in NCP in summer of 2013 (from 11 June to 7 July) in this study. The different temporal and spatial distributions of SO₂ and NO₂ vertical column density (VCD) over this area are characterized under various wind fields. The results show that transport from southern NCP strongly affects air quality in Beijing, and the transport route, particularly SO₂ transport
25 of Shijiazhuang–Baoding–Beijing is identified. In addition, the major contributors to SO₂ along the route of Shijiazhuang–Baoding–Beijing are elevated sources and low area sources for route of Dezhou–Cangzhou–Tianjin–Beijing are found using the interrelated analysis between in situ and mobile DOAS observations during the measurement periods. Furthermore, the discussions of hot spot near JiNan city show that average observed width of polluted air mass is 11.83 km and 17.23 km associated with air

mass diffusion, which is approximately 60 km away from emission sources based on geometrical estimation. Finally, a reasonable agreement exists between OMI and mobile DOAS observations with correlation coefficient (R^2) of 0.65 for NO_2 VCDs. Both datasets also have similar spatial pattern. The fitted slope of 0.55 is significantly less than unity can reflect the contamination of local sources and
5 OMI observations need to improve the sensitivities to the near-surface emission sources through the improvements of retrieval algorithm or resolution of satellites.

1. Introduction

Driven by the unprecedented economic growth and explosive increase in urbanization, China has been
10 experiencing severe air pollution, particularly in developed areas, such as, Yangtze River Delta region and Pearl River Delta region (van Donkelaar et al., 2010). The severe haze pollution events occurred frequently since the end of 2012 in Jing-Jin-Ji region, including Beijing, Tianjin, Shijiazhuang, and some cities in Hebei province. Long duration, heavy pollution level, and large spread area are main characteristics of haze pollution, which have been rare in the past decades (Sun et al., 2014; Ji et al.,
15 2014; Zhao et al., 2013). Haze pollution has affected the health and lifestyle of millions, drawing extensive worldwide attention on China. Severe air pollution in Beijing, the capital of China, has troubled the public, scholars, and the government. Concurrently, many studies have been conducted in Beijing and its surrounding areas (Wang et al., 2014a; Wang et al., 2014b; Xu et al., 2011; Ma et al., 2012). Related results show that the air pollution in Beijing is a regional environmental problem caused
20 by the influences of both local emission and external transport (Ying et al., 2014; Guo et al., 2014; Wu et al., 2011).

NO_2 is one of the most important atmospheric trace gases. It plays a key role in tropospheric and stratospheric chemistry and strongly participates in the chain reaction formation of tropospheric ozone (Crutzen et al., 1970). Moreover, NO_2 is a main pathway of OH loss, which determines the atmospheric
25 oxidative capacity, under heavy polluted conditions (Finlayson-Pitts et al., 1999; Kanaya et al., 2014). Aside from NO_2 being generally harmful to human health, long-term NO_2 exposure in high concentrations can also increase the possibility of bronchitis in asthmatic children (WHO, 2006). Combustion processes, such as power generation and release of pollutants from vehicles, are the major sources of anthropogenic NO_2 emissions. Meanwhile, SO_2 is a colorless gas that adversely affects the
30 respiratory system. Emissions from elevated releases, such as that from power plants, are the main

contributors for anthropogenic SO₂ emission (Xu et al., 1998; Ramanathan et al., 2003). Furthermore, NO₂ and SO₂ are important precursors of aerosol. Under suitable meteorological conditions, NO₂ and SO₂ tend to form nitrate and sulfate, which contribute to the formation of secondary aerosols (Jang et al., 2001; Boichu et al., 2015). Some studies show that nitrate and sulfate account for nearly 38% in particulate matter (PM_{2.5}, with aerodynamic diameter less than or equal to 2.5μm), which is an important element of haze, in Jing-Jin-Ji region (Huang et al., 2014; Yang et al., 2011, Sun et al., 2013, Zhang et al., 2013). Based on model simulation, PM_{2.5} concentration can be declined by 13% if SO₂ and NO_x emission have been controlled effectively (Zhao et al., 2013a). In addition, the spatial and temporal distribution of SO₂ and NO_x (nitrogen oxides, sum of NO and NO₂, NO_x=NO+NO₂) vary significantly (Lee et al., 2009; Matsui et al., 2009; Wang et al., 2009). To investigate the spatial and temporal distribution of SO₂ and NO₂ and evaluate the influence of transport on Beijing, the observations of distribution of tropospheric SO₂ and NO₂ VCDs were conducted in NCP using mobile DOAS from June to July 2013. NCP is located in northern China, surrounded by Taihang Mountain (at the west of NCP), Yanshan Mountain (at the north of NCP) and Bohai Sea (at the east of NCP). NCP consists of the Jing-Jin-Ji region and other provinces in Northern China and is one of the heaviest polluted areas in China (Quan et al., 2011).

A large number of studies on distributions of air pollutants have been performed in NCP. The characteristics of concentration and evolution at different sites and formation mechanisms during heavy pollution periods have been researched using ground-based observation networks (Hu et al., 2014).

Meanwhile, regional variations of gases, particle pollutants, and other factors which influence pollution characteristics have been detected using airborne measurement (Zhang et al., 2014). Also, based on measurements using a mobile laboratory, Wang et al. (2011) analyzed the regional distribution of SO₂ in Beijing and its surrounding areas and estimated transport flux from the outside to Beijing (Wang et al., 2011). Model simulations, another method, can obtain distribution, transboundary transport fluxes, and major transport channels of Beijing in combination with meteorological data (An et al., 2012).

However, current studies mainly focus on ground-based observations, lacking stereoscopic monitoring data that can help better understand the source and transport of air pollution.

Mobile DOAS provides another remote sensing method to obtain stereoscopic monitoring data and characterize regional distribution of air pollution over medium- to large-distance scale. This technique can detect the horizontal distribution of pollutants with high spatial-temporal resolution and rapidly

identify the locations of pollution sources. Furthermore, information on the upper layer of air pollution can be investigated. Thus, transport of air pollution can be analyzed and associated with meteorological trajectory data. At present, some related studies have been carried out (Ibrahim et al., 2010; Shaiganfar et al., 2011 and 2015). In China, several measurements are also performed in Shanghai and Guangzhou.

5 Wang et al. (2012) evaluated the NO_2 variations over the central urban area before and after Shanghai Expo 2010 (Wang et al., 2012). Wu et al. (2013) observed the distributions and emissions of SO_2 and NO_2 in Guangzhou Eastern Area during Guangzhou Asian Games 2010(Wu et al., 2013). However, this study is to summarize the distributions of SO_2 and NO_2 , verify the type of air pollution sources, and to discuss potential of transport from NCP to Beijing over NCP area. In addition, the mobile platform
10 referred in this study is also equipped with some in-situ instruments from Peking University (PKU) to synchronously measure near-surface concentration of gases and particulate mass.

In this paper, we present the observations of SO_2 and NO_2 VCDs in NCP from June to July 2013 using mobile DOAS, and the distributions of SO_2 and NO_2 VCDs in NCP are characterized. In combination with in-situ data, the characteristics of SO_2 and NO_2 along southwest and southeast pathway under
15 different wind fields are characterized and the hot spots and their possible sources along the measurement paths are determined. The pollution transport pathways to Beijing are revealed and first time convinced by capturing the plume. Finally, the NO_2 VCDs from mobile DOAS data are compared with those from Ozone Monitoring Instrument (OMI). Obtained data are in good agreements.

This paper is organized as follows: the experimental process, including overview of the measurements
20 and instruments. Wind fields and the principle of retrieval of vertical column densities of tropospheric trace gas are discussed in detail in Sect. 2. Section 3 gives us the results and discussions, including distributions of SO_2 and NO_2 tropospheric VCDs over NCP and analysis of hot spot and comparison with OMI NO_2 . Finally, the conclusions are presented in Sect. 4.

25 **2. Experimental**

2.1 Overview of the measurements

To characterize spatial distributions of SO_2 and NO_2 VCDs and investigate potential transport to Beijing, the measurement routes are specially designed. The entire measurement period from 11 June to 16 July 2013 is initially divided into five identical cycles. Mobile DOAS observations span four cycles
30 (from 11 June to 7 July) and cover four different routes because of bad weather or vehicle problems.

Figure 1 depicts the detailed routes of mobile DOAS measurements. Cycle 1 covers five routes with a total path of 1400 km and takes five days to complete. The five routes are Beijing (BJ) to Shijiazhuang (SJZ), Shijiazhuang to Dezhou (DZ), Dezhou to Baoding (BD) to Cangzhou (CZ), Cangzhou to Zhuozhou (ZZ), and Zhuozhou to Beijing for Cycle1. Due to the bad weather or vehicle problems, 5 Cycles 2 and 3 took four and three days to complete, resulting in skipping of some routes. We needed one more day to complete Cycle 4 due to power failure on 4 July. The details of monitoring information are listed in Table 1.

The approximate starting and ending times are 10:00 and 14:00 (Local Time, LT), particularly considering stable boundary layer and battery endurance. The temperature varied from 30 °C to 36 °C 10 and the wind fields were dominated by south and north. Some other meteorological parameters, e.g. humidity and pressure are in the range of 32% ~61% and 994hPa~1009hPa during the entire measurement period.

2.2 Instrument description

Mobile DOAS instrument collects scattered sunlight from zenith observation. Details of the instrument 15 and performances are described in our previous study (Wu et al., 2013). Briefly, the system consists of telescope, a miniature fiber spectrometer unit, global positioning system, and computer. The series of Ocean Optics HR2000 is selected as miniature spectrometer, with spectral resolution of 0.6 nm and spectral range of 290 nm to 420 nm. The spectrometer is stored in a temperature-controlled unit to stabilize the temperature at $+30\pm 0.1$ °C to avoid spectral shifts caused by temperature variations. The 20 detection limits of the instrument is approximately $3\text{--}5 \times 10^{15}$ molec./cm² for SO₂ and NO₂. The instrument is installed on a van, which is a mobile laboratory platform from PKU (Wang et al., 2009, 2011). The mobile DOAS system is powered by 220V alternating current through conversion of +12V direct current battery with a power converter.

In addition, PKU has set up some in-situ instruments on the van, including SO₂ analyzer (ECOTECH 25 9850A), NO_x analyzer (ECOTECH 9841A), CO analyzer (ECOTECH 9830A), ozone analyzer (ECOTECH 9810A), and CO₂ analyzer (ECOTECH 9820A). Aside from gaseous pollutant instruments, some aerosol instruments, such as GRIMM and Dusttrak for PM_{2.5} and Fast Mobility Particle Sizer, were also available onboard for analysis of particle size distribution. The details of the setup and performance of the instruments are described in Wang et al. (2009, 2011).

30 2.3 Backward Lagrangian Trajectory Simulation

Apart from the near-surface wind data, the backward trajectory of air mass from the stations in Beijing was also simulated using the Hybrid Single Particle Lagrangian Integrated Trajectory model (HYSPPLIT, offline version), which has been developed by the Air Resources Laboratory of the US National Oceanic and Atmospheric Administration. An average boundary layer height (BLH) of around 1000m has been calculated during noontime in summer over NCP area by Lv et al, 2017, based on lidar observations. The middle altitude of BLH, i.e., 500m, is taken as the representative horizontal transport height to investigate transport effect on an assumption of well mixing throughout the whole BLH around noontime. Backward trajectories were calculated once every 2 h for 1 day (24 h) at a selected altitude of 500 m above ground level for each cycle. An archive meteorological database with a horizontal resolution of $1^{\circ} \times 1^{\circ}$ from the Global Data Assimilation System, which is enough to identify the original regions of air mass, is chosen to run the HYSPPLIT model.

Figure 2 shows the cluster average backward trajectory for Cycles 1, 2, 3, and 4. During the measurement periods of Cycles 1 and 3, all air masses come from the southern regions. For Cycle 2, the mean back trajectory is roughly split equally between north and south. However, the dominant wind field is north during the mobile DOAS observations for Cycle 2, except for the wind on 21 June as listed in Table 1. A small different wind field is present for Cycle 4. The north wind account for nearly 72% and the south wind 28%. Maybe there are some differences from the wind data as listed in Table 1 for Cycle 4. Two main reasons can account for the differences. Firstly, the backward trajectories are simulated at Beijing site and this ratio represents Beijing area. Secondly, the ratio results from calculations of 60 trajectories in five days for Cycle 4. However, the wind data described in Table 1 focuses on the time of mobile DOAS observations. In general the wind fields are variations in NCP for Cycle 4 and the specific observation time of mobile DOAS exhibit that dominant wind is south except for that on 2 and 5 July.

2.4 Retrieval of Vertical Density of Tropospheric Trace Gas

SO₂ and NO₂ column densities are retrieved from zenith sky mobile DOAS with WinDOAS software. Each measured spectrum is divided through Fraunhofer reference spectrum (FRS) after dark current and offset corrections. One FRS spectrum, a relative “clean-air” spectrum, is selected to retrieve all other measured spectra during the whole field campaign. The FRS is recorded at approximately 11:30 LT on April 30, 2013 near Bohai Sea, considering strong wind and good air quality on that day (see Fig. 1a). [The spectral evaluation applied to each measurement spectrum starts with dark current and offset](#)

corrections, followed by the division with a FRS spectrum. A high-pass filter is applied to the logarithm of this ratio. Differential slant column densities (DSCD, which is relative to the value of Fraunhofer spectrum), are then obtained by fitting narrow band spectral absorption cross sections to the processed measurement spectra. Fit examples for NO₂ and SO₂ are illustrated in Fig. 3.

5 For the retrieval of SO₂, a fitting window of 310-324 nm is used and for NO₂, a fitting window of 338-370 nm is used, both adapted from experiences during our previous work (Wu et al., 2013) and MAD-CAT (http://joseba.mpch-mainz.mpg.de/mad_cat.htm) intercomparison campaign. The synthetic Ring spectrum is yielded from FRS spectrum using DOASIS software (Kraus, 2006). The slit function is generated from emission peak of mercury lamp at 334 nm. The high-resolution solar spectrum
 10 (Kurucz et al., 1984) is used to calibrate wavelength. The setting and fitting absorbers are summarized in detail in Table 2. The fit uncertainties of NO₂ and SO₂ for the spectrum, as shown in Fig. 3, are approximately 2.48% and 1.84%. The typical uncertainties are less than 15% for NO₂ and 20% for SO₂. The above obtained the DSCDs with respect to FRS spectrum. Tropospheric NO₂ is $\sim 5 \times 10^{15}$ molec./cm² at the location of FRS spectrum on 30 April, 2013 from OMI result. Given the poor
 15 SO₂ satellite data, we checked the SO₂ results at ground level from local environmental protection agency on that day. Compared with the high pollution over NCP area, we neglected these relatively small tropospheric contents in FRS spectrum. As a result, the tropospheric NO₂ and SO₂ VCDs can be calculated with air mass factor (AMF) using following formula (Hönninger et al. 2004):

$$VCD_{trop} = \frac{SCD_{trop}}{AMF_{trop}} = \frac{DSCD + SCD_{FRS} - SCD_{strat}}{DAMF + AMF_{FRS} - AMF_{strat}} = \frac{DSCD_{trop}}{AMF_{trop}} \quad (1)$$

20 The radiative transfer model McArtim (Deutschmann et al., 2011) based on the Monte Carlo method is used to calculate the AMF_{trop} . We assume that aerosol and trace gas profiles are homogeneous below the BLH, whereas exponential profiles are above. Here, the constant concentrations within 1000m of boundary layer are assumed to be approximate 40 ppb and 10 ppb for NO₂ and SO₂ according to state-controlled air-sampling sites. This hypothesis can lead to less than 5% uncertainty based on a
 25 sensitivity study by varying the setting of NO₂ and SO₂ setting. The average aerosol optical density (AOD) of 1.0 is estimated from AERONET on June and July, 2013 at Xianghe site. The profiles of aerosol, NO₂, and SO₂ are taken from LOWTRAN database and US standard atmosphere above the boundary layer. We estimate the total retrieval errors of NO₂ VCDs and SO₂ VCDs to be less than 20%

and 25% (Wu et al., 2013).

3. Results and discussions

3.1 Distributions of SO₂ and NO₂ Tropospheric VCDs over NCP

In this section, the distributions of SO₂ and NO₂ tropospheric VCDs over NCP area are discussed with mobile DOAS observations. First, the overall distributions of SO₂ and NO₂ tropospheric VCDs along the measurement routes under different dominant winds are characterized. Furthermore, we analyze the spatial and temporal variations of SO₂ and NO₂ tropospheric VCDs along the southwest routes (Shijiazhuang–Baoding–Beijing) and southeast routes (Dezhou–Cangzhou–Tianjin–Beijing) for different wind fields. The possible transport route of trace gas is identified using these distribution characteristics.

3.1.1 Overall Distributions of SO₂ and NO₂ Tropospheric VCDs

Each cycle measurement takes four to five days to complete, and this can lead to the probed air mass change when meteorological condition varies rapidly. However, as described in Sect. 2.3 and listed in Table 1, the dominant wind field as a main influencing factor on air mass variation has not significantly changed, particularly the dominant wind direction of southerly and northerly winds during the measurement periods for mobile DOAS. However, air mass variation can also be affected by some other factors (e.g. temperature, humidity and pressure, as discussed in Sect. 2.1), but the atmospheric physical reaction processes is too complicated to discuss in this study. Thus, we assume that, in this work, the air mass does not change dramatically for each cycle measurements.

Typical spatial distributions of SO₂ and NO₂ VCDs along the measurement route over NCP area for north and south wind fields are shown in Fig. 4 (The results for Cycle 3 and Cycle 4 are shown in Fig. S1). The maps of SO₂ in Fig. 4 show that increased values are observed under southerly wind, particularly the results along Taihang Mountain, which is also part of the southwest measurement route (Shijiazhuang–Baoding–Beijing). The high SO₂ VCDs detected in the region near the cities of Shijiazhuang and Baoding city indicate that these regions have emission sources of SO₂. In addition, high SO₂ VCDs are also observed on the cross-section of south route, particularly near JiNan city. This hot spot can always be found under southerly wind during the field campaign, suggesting a strong emission outside the measurement area and south of it. Based on the backward trajectory analysis, the big air pollution plume comes from Liaocheng city, which is another small city close to JiNan western region. Furthermore, relatively low SO₂ VCDs are observed along the southeast route compared with

that of the southwest route.

However, for the northerly wind, no significant increased SO₂ VCDs are noted along the Taihang Mountain. The hot spot near JiNan city are also less pronounced. The downwind SO₂ VCDs of Shijiazhuang and Tianjin city are relatively high due to source emission near the city. The results of comparison of wind direction from south versus north further suggest that the strong emission sources located at the southern region of the measurement area have a significant influence on Beijing under southerly wind, particularly along the Taihang Mountain.

Unlike SO₂, no significant difference between the southerly and northerly wind for NO₂ VCDs is noted. The NO₂ VCDs are affected by local emissions within the cities. High NO₂ VCDs are obtained near Beijing, Baoding, Shijiazhuang and Tianjin city. The same is noted for SO₂, and due to strong emission source contribution, enhanced NO₂ VCDs are also found near JiNan city for south wind field.

3.1.2 Spatial and temporal variations of SO₂ and NO₂ along southwest and southeast routes under different wind fields

As detailed in above analysis, the characteristics of SO₂ and NO₂ distributions have significant variations, including spatial and temporal differences along the southwest and southeast measurement routes. This section firstly investigates the SO₂ and NO₂ characteristics along southwest and southeast routes and then compares them with the results under southerly and northerly wind.

Table 3 lists the SO₂ and NO₂ VCDs from mobile DOAS and near-surface concentrations from in-situ measurements under southerly and northerly wind along the southwest and southeast routes. For the southwest measurement route, the mean VCDs of SO₂ and NO₂ are 4.22×10^{16} molec./cm² and 1.69×10^{16} molec./cm². The mean near-surface concentrations are 9.74 ppb and 111.28 ppb for SO₂ and NO₂. For the southeast measurement route, the mean VCDs of SO₂ and NO₂ are 3.40×10^{16} molec./cm² and 1.15×10^{16} molec./cm². The mean near-surface concentrations of SO₂ and NO₂ are 17.27 ppb and 117.97 ppb, respectively. The VCDs along southwest route are higher than that along the southeast route. However, the near-surface concentration along the different routes is reverse.

The vertical column and in-situ measurements are discussed simultaneously in Table 3. It is interesting to note that such discussions can provide comprehensive information about surface emission and tropospheric pollution. We can also calculate the depth of a layer of air using in-situ mixing ratio and vertical column on the assumption of homogenous mixing within the planetary boundary layer (Chen et al., 2009). However, the height of the layer could not be estimated in this way in this study because the

in-situ measurements contaminated by very local vehicle emission, especially for NO₂. The traffic exhaust is one of the major contributors to NO₂ and large traffic emission result in the inhomogenous mixing within the planetary boundary layer, so it is found that the NO₂ layer would be something like only 30 to 60m thick using above analysis method, which is very unreasonable compared to normal situations. In contrast, the SO₂ layer would vary from about 0.5 to 2.0 km thick, which is in the normal range.

The comparisons of VCDs between different wind fields show that the VCDs under southerly wind are much higher than that under northerly wind along the southwest route, particularly for SO₂, with the value of 6.09×10^{16} molec./cm² and 2.35×10^{16} molec./cm². However, this phenomenon is not obvious along the southeast route. In addition, the comparisons of SO₂ near-surface concentration suggest that the difference between the different wind fields is less pronounced along the southwest route, but is enhanced dramatically along the southeast route under southerly wind, with the value of 23.29 ppb versus 11.24 ppb under northerly wind.

3.1.3 Characterization of emission sources and identification of transport route

Both results from mobile DOAS and in-situ instruments observations for every measurement day are shown in Fig. 5 to Fig. 8. According to the “Box-Chart” plot, some distinct peak values of SO₂ VCDs are measured in the case of south wind, whereas this is not significant for SO₂ near-surface concentration, as shown in Fig. 5. These findings indicate that the elevated sources existed in the southwest of measurement region, and the elevated sources are the main SO₂ sources for this region. We could also infer that the high SO₂ value may be located in the upper layer. Moreover, we further investigate the potential locations of main SO₂ sources for this region. For the north wind, downwind peaks are found near Shijiazhuang city and thus sources of SO₂ within the encircled cycles, but closer to the southern measurement route, can be identified (S1 in Fig. 4). In addition, a slight increase in southern region of Baoding city, so that we infer a SO₂ source lies in the south of Baoding city (S2 in Fig. 4). The maps for SO₂ in Fig. 4 show downwind peaks along the southwest measurement route when the wind comes from south, suggesting important SO₂ emission sources are outside the cycles (S3 in Fig. 4). No significant peak values for NO₂ VCD (see Fig. 6) are noted. However, we found them on near-surface concentrations, such as on 11 June. The results show that the traffic emission located at the near surface is the main sources of NO₂. If we traverse areas with large volumes of vehicles, the NO₂ near-surface concentrations should increase.

For the southeast measurement routes, we did not observe the peak values of SO₂ VCDs and near-surface concentrations, as shown in Fig. 7. One interesting finding is that the SO₂ VCD on 21 June increased slightly from “Box-Chart” plot in Fig. 7. The analysis of 24h backward trajectory of 500m on 21 June in Cangzhou city (the location of peak value), we found the air mass come from west/southwest direction near mobile DOAS measurement time (near-surface wind direction dominated by west), but from northeast direction when the time moves forward longer in Cangzhou city as shown in Fig. S2. So, I think the higher SO₂ VCD on 21 June maybe caused by local emission and transport from northeast direction. In general, these findings verify that the low nonpoint sources are the main contributors in the southeast of measurement region.

As shown in Fig. 8, the NO₂ VCDs for south wind are 1.38 times higher than that for north wind, but the near-surface concentrations are almost equal for these two different winds. The same is true for SO₂; we also did not find elevated NO₂ sources in the southeast of measurement region.

Based on the above analysis, we could infer that the pollution source in the southwest and southeast regions have two types. The finding is also proven by the emission inventory: several large emission sources are located southwestern region, and some near-surface fugitive sources are located southeastern region (Wang et al., 2011).

Similar with SO₂, the average NO₂ VCD along the southeast route is lower than that along the southwest route, but the near-surface concentration is higher than that along the southwest routes. The near-surface vehicle emissions are the major contributors of NO₂, and fugitive emission sources are additional sources of NO₂. In addition, the high NO₂ near-surface concentration along the southeast route indicates large traffic volume over this region. This is also consistent with the fact that the southeast route is an expressway from Beijing to Shanghai, the two most economically developed cities in China. Additionally, trade exchanges among these two and other cities are frequent.

The VCDs and near-surface concentrations of SO₂ and NO₂ are high under southerly wind in most cases, particularly for SO₂ VCDs along the southwest routes and SO₂ near-surface concentrations along the southeast routes. From mobile DOAS observations, significant variations of SO₂ VCDs along the southwest routes (also along Taihang Mountain) are shown in Fig. 9. The variations of SO₂ VCDs for different wind fields indicate that the southwest route is a transport route of SO₂ for Beijing. When the air plume comes from the south, the air quality in Beijing deteriorates. Figure 10 shows the mean SO₂ concentrations for the time when south or north wind is dominant in Beijing. The monitoring data in

seven state-controlled air-sampling sites demonstrate that the average SO₂ concentrations ranged from 8.22 ppb to 13.04 ppb for south wind and from 3.71 ppb to 5.02 ppb for north wind during the mobile DOAS observation periods in the Beijing area. Previous studies also confirmed the presence of this transport route using other methods (Su et al., 2014). This work not only identifies the transport route of SO₂ with mobile DOAS observations, but also determines the high SO₂ concentration existing in the upper layer combination the concurrent in-situ data.

3.2 Analysis of hot spot

The hot spots are observed for the route of Shijiazhuang–Dezhou measurements under southerly wind. The maximum SO₂ VCD and NO₂ VCD can reach 4.84×10^{17} molec./cm² and 7.41×10^{16} molec./cm². However, they are less pronounced for north wind. Figures 11 and 12 present the results of SO₂ and NO₂VCDs for the Shijiazhuang–Dezhou measurements under southerly and northerly wind.

Figure 11 exhibits a large polluted air mass coming from southern region in the rectangular area [Fig. 11 (a1) and Fig. 11(b1)] under the southerly wind on 12 June. First, this air mass led to the rapid enhancement of SO₂ and NO₂ VCDs in Area I and Location 1 [Fig.11 (a1), (a2), (b1), and (b2)]; then, the VCDs in Area II and Location 2 increased subsequently due to the air mass diffusion. The time series of SO₂ and NO₂ VCDs tell us that with the increase of distance, the peak value decreased in Area II and observed width of air mass enlarged because of air mass diffusion. For Area I, the peak values of SO₂ and NO₂ VCDs are 4.43×10^{17} molec./cm² and 6.80×10^{16} molec./cm² at 13:02 (LT). However, the peak value for SO₂ and NO₂ decreased to 3.44×10^{17} molec./cm² and 4.68×10^{16} molec./cm² in Area II at 13:43 (LT).

Furthermore, observed widths of air mass are estimated in Area I and Area II from the time series of SO₂ VCDs in Fig. 10 (a3) using following formula:

$$W = \sum_i (t_{i+1} - t_i) \cdot \bar{V}_{i+1 \rightarrow i} \quad (2)$$

where i is the number of spectrum in Fig. 11(a3), t_{i+1} and t_i are the time for the spectrum of i and $i + 1$, and $\bar{V}_{i+1 \rightarrow i}$ is the mean car speed between t_{i+1} and t_i .

Using the above formula, the average observed width of air mass is calculated to be 11.83 km in Area I and 17.23 km in Area II. Combined with the observed widths for Areas I and II and the geometric relationships between these two locations, the distance of the air pollution sources from the Area I is estimated at a distance of approximately 61.39 km. The distance of Area I from Liaocheng city is

approximately 60 km, proving that the source is indeed from Liaocheng direction, as discussed in Sect. 3.1.1.

While the above peak values are less pronounced under the northerly wind on 18 June as shown in Fig. 12, this phenomenon further confirmed large sources located at the southern region outside the measurement area. When the dominant wind comes from south, the air quality of the measurement area is severely influenced by the sources.

In addition, we simultaneously compare the one-minute average VCDs results with the one-minute near-surface concentrations along the Shijiazhuang–Dezhou routes. Figure 13 shows the time series of VCDs and near-surface concentrations for SO₂ and NO₂ along the measurement route under southerly and northerly wind. For the specific southerly wind, such as on 3 July, the high SO₂ and NO₂ VCDs were captured through mobile DOAS in the areas, as shown in Fig. 11 (a2) or (b2) (the area marked with sparse rectangular box in Fig. 13). This also indicates that the polluted air mass contained high levels of SO₂ and NO₂. Furthermore, from the time series observations of SO₂ near-surface concentrations, high near-surface concentrations are observed simultaneously in the sparse rectangle, as shown in Fig. 13 (a), and this is the same as SO₂ VCDs. The combined results demonstrate that part of the air mass have deposited, resulting in the increase of SO₂ near-surface concentrations. However, one interesting thing has been found the NO₂ near-surface concentrations do not significantly increase in this area [Fig. 13 (b)]. Following the above explanation regarding SO₂, the declined air mass is supposed to cause an increase in NO₂ near-surface concentration. The lifetime of NO₂ is less than SO₂, and the NO₂ conversion to other species, such as nitrate, could account for this unexpected finding. For the northerly wind, both VCDs and near-surface concentrations do not increase obviously in the sparse box area. The correlation analysis between NO₂ and CO near-surface concentrations (Fig. 14) shows that NO₂ near-surface concentration mainly results from vehicle exhaust, although the correlation coefficient under southerly wind slightly better than that under northerly wind during the measurement periods.

3.3 Comparison with OMI NO₂

OMI is onboard the Aura satellite of the Earth Observing System, was launched on 15 June 2004 with a nadir viewing mode (Levelt et al., 2006). OMI can be used to monitor global atmospheric NO₂ distribution with high spatial (up to 13 × 24 km) and temporal (daily global coverage) resolution. OMI is equipped with two charge-coupled devices spanning a wavelength range from 264 nm to 504 nm to

measure spectra of scattered sunlight in the ultraviolet and visible spectra. The overpass time of OMI is 13:45 (LT) on the ascending node. In this study, the OMI tropospheric NO₂ data product from NASA is used. The data analysis consisted of three steps to derive tropospheric NO₂ VCDs. The SCDs of NO₂ are derived from OMI collected spectra based on DOAS method in the wavelength ranging from 405 nm to 465 nm. And then the AMFs are applied to convert the SCDs to VCDs with monthly average NO₂ profile shapes (Rotman et al., 2001). Finally, the stratospheric contribution is estimated to derive tropospheric NO₂ VCDs by subtracting the stratospheric columns. Detailed description of tropospheric NO₂ retrieval process can be found in Bucsela et al. (2013).

In this study, to achieve a better comparison between OMI and mobile DOAS, the OMI tropospheric NO₂ data are gridded onto a 0.1°×0.1° grid with an error and area weighted gridding algorithm (Wenig et al., 2008). The cloud fraction of 0.4 is used as a threshold to filter out the data. As a result, a total of 8 days (11, 12, 13, 18, 25, and 26 June and 3 and 6 July with a cloud cover lower than 0.4) of measurements from both OMI and mobile DOAS can be used for data comparison.

The comparisons of NO₂ VCDs between both datasets for the 8-day measurement are shown in Fig. 15. The similar spatial patterns are detected by both OMI and mobile DOAS observations. In most cases, high level of NO₂ VCD is observed around Shijiazhuang area. However, the hot spots of mobile DOAS observations, as shown in Sect. 3.2, cannot be detected completely using OMI due to the insensitivity of OMI observation to near-surface sources. We also found that the NO₂ VCDs along southwest route are higher than that along the southeast route from OMI observations, the same as discussed in Sect. 3.1.2.

Moreover, the mobile DOAS data are averaged within each gridded satellite pixel (0.1°×0.1°) and compared to OMI values within each pixel. The correlation analysis for all the datasets of the 8-day measurements is shown in Fig. 16. The error bars indicate the OMI error and the standard deviation of mobile DOAS observations within above pixel, which are also taken into account when performing the linear regression. The correlation coefficient (R^2) is 0.65, suggesting that both observations agree reasonably well. However, a systematic difference between the mobile DOAS and OMI NO₂ VCDs, implied by the fitted slope of 0.55, is exist as shown in Fig. 16. These discrepancies can be attributed to source emission from near surface (e.g. traffic exhaust, industrial sources etc.) or lower troposphere (e.g. elevated sources). Due to the limited spatial resolution and shield by aerosols and clouds, the OMI observations are insensitivity to these sources. However, the mobile DOAS have an ability of rapid

response to that, especially for lower troposphere, like elevated sources. Also some studies have shown that OMI NO₂ VCDs are systematically smaller than mobile DOAS and MAX-DOAS observations over polluted areas (Shaiganfar et al., 2011, Chan et al., 2015). Of course, some other factors can also result in these differences, like NO₂ diurnal cycle. Previous studies (Wu et al., 2013) have shown that the strong diurnal variations of NO₂ occur between 10:00 and 11:00. This study, our mobile DOAS measurements are carried out approximately from 10:00 to 14:00, and the OMI overpass time may be 13:45. As a result, the time mismatch between OMI and NO₂ could result in different NO₂ VCDs. In addition, the NO₂ VCDs of OMI and mobile DOAS need to be converted from SCDs with AMFs. The calculations of AMFs should consider the trace gas profiles, aerosol profiles, ground albedo and wavelength etc. So, the different hypothesis on calculation of AMFs can also yield different VCDs.

4. Conclusions

The NCP has been experiencing severe air pollution associated with unprecedented economic boom and accelerated urbanization over the past few years. To characterize the temporal and spatial distributions and to investigate the effect of various sources on air quality, particularly for Beijing, the observations of tropospheric SO₂ and NO₂ VCDs through mobile DOAS are performed from 11 June to 7 July 2013.

Combined with the simultaneously measurements of near surface concentrations through in-situ instruments, the various temporal and spatial distributions of SO₂ and NO₂ under different wind fields are discussed. For the southwest measurement route, the mean SO₂ VCD under southerly wind is 6.09×10^{16} molec./cm², which is 2.6 times higher than that for north wind (2.35×10^{16} molec./cm²). The near-surface SO₂ concentration under southerly wind is 1.24 times higher than that under northerly wind, with the value of 10.78 ppb and 8.69ppb. Except for SO₂, the mean NO₂ VCD and near-surface NO₂ concentration under southerly wind are 1.77 and 1.42 times higher than that under northerly wind. The significant discrepancies of SO₂ VCD between the two various wind indicate that the transport from southern NCP area strongly affects the air quality over northern NCP area (like Beijing). And the primary contributors to SO₂ in the southwest of measurement region are elevated emission sources, like power plant and steel company etc. using the interrelated analysis of VCDs and in-situ data. Moreover, the transport route of the path (Shijiazhuang-Baoding-Beijing) is identified.

However, for the southeast measurement route, we did not find a distinct difference of SO₂ VCDs

under different wind fields, with the value of 3.29×10^{16} molec./cm² and 3.51×10^{16} molec./cm² for south and north wind. The mean near-surface concentration of SO₂ for southerly wind is nearly double than that of the value under northerly wind, with the concentration of 23.29 ppb and 11.24 ppb. The NO₂ VCDs and near-surface concentrations along the southeast route also do not have significant variations. Under south wind, the NO₂ VCD and near-surface concentration are 1.34×10^{16} molec./cm² and 119.12 ppb. Under north wind, the NO₂ VCD and near-surface concentration are 9.68×10^{15} molec./cm² and 116.82 ppb. The higher SO₂ near-surface concentration along the southeast route indicates the low area sources are the primary contributors to SO₂ rather than elevated sources. Analysis of hot spot shows that the average observed width of air mass is 11.83 km and 17.23 km associated with air mass diffusion. Another interesting finding is that the NO₂ near-surface concentration did not significantly enhance for the area of air mass. The lifetime of NO₂ is less than that of SO₂ and NO₂ conversion to other species could account for this unexpected findings. The correlation analysis between NO₂ and CO near-surface concentrations shows that NO₂ near-surface concentration mainly resulted from vehicle exhaust.

Furthermore, comparison with OMI NO₂ VCDs indicates a reasonable agreement between OMI and mobile DOAS with correlation coefficient (R^2) of 0.65. Both datasets have similar spatial patterns. In most cases, the high level of NO₂ VCDs is observed around Shijiazhuang area. However, the fitted slope of 0.55 is significantly less than unity may reflect the existence of some near surface local sources which are insensitive observations or underestimation by OMI. This study will promote the development and extend mobile DOAS technique to rapidly capture the regional distribution of air pollutants and evaluate the potential transport as well as the use of satellite validation.

Acknowledgements: The authors would like to thank Prof. Zhu's group from Peking University for the arrangements of the experiments and providing the data from in-situ instruments during the CAREBEIJING 2013 field campaign. This work was also made possible by the support of the National Natural Science Foundation of China (41530644 and 41605013), National Key R&D Program (2016YFC0208203 and 2016YFC0201507) and Anhui Province Natural Science Foundation of China (1508085QD71).

30 **References**

- An, J. L., Li, J., Zhang, W., Chen, Y., Qu, Y., Xiang, W. L.: Simulation of transboundary transport fluxes of air pollutants among Beijing, Tianjin, and Hebei Province of China, *Acta Scientiae Circumstantiae*, 32(11) : 2684-2692, 2012.
- Boichu, M., Clarisse, L., P    J.-C., Herbin, H., Goloub, P., Thieuleux, F., Ducos, F., Clerbaux, C., and
5 Tanr  , D.: Temporal variations of flux and altitude of sulfur dioxide emissions during volcanic eruptions: implications for long-range dispersal of volcanic clouds, *Atmos. Chem. Phys.*, 15, 8381–8400, 2015.
- Bucsela, E.J., Krotkov, N.A., Celarier, E.A., Lamsal, L.N., Swartz, W.H., Bhartia, P.K., Boersma, K.F.,
10 Veefkind, J.P., Gleason, J.F., Pickering, K.E.: A new stratospheric and tropospheric NO₂ retrieval algorithm for nadir-viewing satellite instruments: applications to OMI. *Atmos. Meas. Tech.* 6 (10), 2607e2626, 2013.
- Bogumil, K., Orphal, J., Homann, T., Voigt, S., Spietz, P., Fleischmann, O. C., Vogel, A., Hartmann, M.,
15 Kromminga, H., Bovensmann, H., Frerick, J., and Burrows, J. P.: Measurements of molecular absorption spectra with the SCIAMACHY preflight model: instrument characterization and reference data for atmospheric remote-sensing in the 230–2380 nm region, *J. Photoch. Photobio. A*, 157, 167–184, 2003.
- Chen, D., Zhou, B., Beirle, S., Chen, L. M. and Wagner, T.: Tropospheric NO₂ column densities deduced from zenith-sky DOAS measurements in Shanghai, China, and their application to satellite validation, *Atmos. Chem. Phys.*, 9, 3641–3662, 2009.
- 20 Chan, K. L., Hartl, A., Lam, Y. F., Xie, P. H., Liu, W. Q., Cheung, H. M., Lampel, J., Pöhlerf, D., Li, A., Xu, J., Zhou, H. J., Ning, Z., Wenig, M. O.: Observations of tropospheric NO₂ using ground based MAX-DOAS and OMI measurements during the Shanghai World Expo 2010, *Atmos. Environ.*, 119, 45-58, 2015.
- Crutzen, P. J.,: The influence of nitrogen oxides on the atmospheric ozone content. *Q. J. R. Meteorol. Soc.* 96 (408), 320-325, 1970.
25
- Deutschmann, T., Beirle, S., Frieß U., Grzegorski, M., Kern, C., Kritten, L., Platt, U., Prados-Roman, C., Pukite, J., Wagner, T., Werner, B., Pfeilsticker, K.: The Monte Carlo atmospheric radiative transfer model McArtim: Introduction and validation of Jacobians and 3D features, *Journal of Quantitative Spectroscopy & Radiative Transfer*, 112, 1119–1137, 2011.
- 30 Finlayson-Pitts, B. J. and Pitts, J. N.: *Chemistry of the Upper and Lower Atmosphere: Theory,*

Experiments, and Applications, Academic Press, San Diego, USA, 1999.

- Guo, S., Hu, M., Misti L, Z., Peng, J., Shang, D., Zheng, J., Du, Z., Wu, Z., Shao, M., Zeng, L., Mario J, M., and Zhang, R.: Elucidating severe urban haze formation in China, PNAS, 111,17373–17378, 2014.
- 5 Huang, R., Zhang, Y., Bozzetti, C., Kin-Fai, H., Cao, J., Han, Y., Daellenbach, K. R., Slowik, J. G., Platt, S. M., Canonaco, F., Zotter, P., RobertWolf, Simone, M. P., Emily, A. B., Monica C., Giancarlo, C., Andrea, P., Margit, S., Gulcin, A., Jurgen, S. K., Ralf, Z., Zhisheng, A., Sonke, S., Urs, B., Imad, E. H., Andre S. H. Prevot: High secondary aerosol contribution to particulate pollution during haze events in China, Nature, 514, 218-222, 2014.
- 10 Hu, J. L., Wang, Y. G., Ying, Q., Zhang, H. L.: Spatial and temporal variability of PM_{2.5} and PM₁₀ over the North China Plain and the Yangtze River Delta, China, Atmos. Environ., 95, 598-609, 2014.
- Hönninger, G., von Friedeburg, C., and Platt, U.: Multi axis differential optical absorption spectroscopy (MAX-DOAS), Atmos. Chem. Phys., 4, 231–254, doi:10.5194/acp-4-231-2004, 2004.
- Ibrahim, O., Shaiganfar, R., Sinreich, R., Stein, T., Platt, U., and Wagner, T.: Car MAX-DOAS
15 measurements around entire cities: quantification of NO_x emissions from the cities of Mannheim and Ludwigshafen (Germany), Atmos. Meas. Tech., 3, 709–721, doi:10.5194/amt-3-709-2010, 2010.
- Lv, L. H., Liu, W. Q., Zhang, T. S., Dong, Y. S., Chen, Z. Y., Fan, G. Q., Liu, Y., Xiang, Y.:
20 Characteristics of Boundary Layer Height in Jing-Jin-Ji Area Based on Lidar, Laser & Optoelectronics Progress, 54, 010101-1~7, 2017. (in Chinese)
- Ji, D. S., Li, L., Wang, Y., Zhang, J., Cheng, M., Sun, Y., Liu, Z., Wang, L. L., Tang, G. Q., Hua, B., Chao, N., Wen, T., Miao, H.: The heaviest particulate air-pollution episodes occurred in northern China in January, 2013: Insights gained from observation, Atmos. Environ., 92, 546-556, 2014.
- Jang, M., Kamens, R.M.: Characterization of secondary aerosol from the photooxidation of toluene in
25 the presence of NO_x and 1-propene. Environ. Sci. Technol. 35 (18), 3626-3639, 2001.
- Kanaya, Y., Irie, H., Takashima, H., Iwabuchi, H., Akimoto, H., Sudo, K., Gu, M., Chong, J., Kim, Y. J., Lee, H., Li, A., Si, F., Xu, J., Xie, P. H., Liu, W. Q., Dzhola, A., Postlyakov, O., Ivanov, V., Grechko, E., Terpugova, S., and Panchenko, M.: Long-term MAX-DOAS network observations of NO₂ in Russia and Asia (MADRAS) during the period 2007–2012: instrumentation, elucidation of
30 climatology, and comparisons with OMI satellite observations and global model simulations,

- Atmos. Chem. Phys., 14, 7909–7927, doi:10.5194/acp-14-7909-2014, 2014.
- Kraus, S.: DOASIS, A Framework Design for DOAS, PhD-thesis, University of Mannheim, Shaker Verlag, Heidelberg, Germany, 2006.
- Kurucz, R. L., Furenlid, I., Brault, J., and Testerman, L.: Solar flux atlas from 296 nm to 1300 nm, National Solar Observatory Atlas No. 1, Office of University publisher, Harvard University, Cambridge, 1984.
- Lee, H. L., Kim, Y. J., Jung, J., Lee, C., Klaus-Peter, H., Platt, U., Hu, M., Zhu, T.: Spatial and temporal variations in NO₂ distributions over Beijing, China measured by imaging differential optical absorption spectroscopy, *Journal of Environmental Management*, 90, 1814–1823, 2009.
- Levelt, P. F., van den Oord, G. H. J., and Dobber, M. R.: The ozone monitoring instrument, *IEEE T. Geosci. Remote*, 44, 1093–1101, 2006.
- Ma, J. Z., Wang, W., Chen, Y., Liu, H. J., Yan, P., Ding, G. A., Wang, M. L., Sun, J., and Lelieveld, J.: The IPAC-NC field campaign: a pollution and oxidization pool in the lower atmosphere over Huabei, China, *Atmos. Chem. Phys.*, 12, 3883–3908, 2012.
- Matsui, H., Koike, M., Kondo, Y., Takegawa, N., Kita, K., Miyazaki, Y., Hu, M., Chang, S.-Y., Blake, D. R., Fast, J. D., Zaveri, R. A., Streets, D. G., Zhang, Q., and Zhu, T., Spatial and temporal variations of aerosols around Beijing in summer 2006: Model evaluation and source apportionment, *J. Geophys. Res.*, 114, D00G13, doi:10.1029/2008JD010906, 2009.
- Meller, R. and Moortgat, G. K.: Temperature dependence of the absorption cross sections of formaldehyde between 223 and 323K in the wavelength range 225–375 nm, *J. Geophys. Res.-Atmos.*, 105, 7089–7101, <https://doi.org/10.1029/1999JD901074>, 2000.
- Quan, J., Zhang, Q., He, H., Liu, J., Huang, M., and Jin H.: Analysis of the formation of fog and haze in North China Plain (NCP), *Atmos. Chem. Phys.*, 11, 8205–8214, 2011.
- Ramanathan, V. and Crutzen, P. J.: New directions: Atmospheric brown “Clouds”, *Atmos. Environ.*, 37, 4033–4035, 2003.
- Rotman, D.A., Tannahill, J.R., Kinnison, D. E., Connell, P. S., Bergmann, D., Proctor, D., Rodriguez, J. M., Lin, S. J., Rood, R. B., Prather, M.J., Rasch, P.J., Considine, D.B., Ramarosan, R., Kawa, S. R.: Global modeling initiative assessment model: model description, integration, and testing of the transport shell. *J. Geophys. Res. Atmos.* 106 (D2), 1669e1691, 2001.
- Su, F. Q., Gao, Q. X., Zhang, Z. G., Ren, Z. H., Yang, X. X.: Transport Pathways of Pollutants from

Outside in Atmosphere Boundary Layer, *Research of Environmental Sciences*, 17,1: 26-30, 2014.
(in Chinese)

Sun, Y., Q. Jiang, Z. Wang, P. Fu, J. Li, T. Yang, and Y. Yin: Investigation of the sources and evolution processes of severe haze pollution in Beijing in January 2013, *J. Geophys. Res. Atmos.*, 119, 4380–4398, doi: 10.1002/2014JD021641, 2014.

Sun, Y. L., Wang, Z. F., Fu P. Q., Yang T., Jiang, Q., Dong, H. B., Li, J., and Jia, J. J.: Aerosol composition, sources and processes during wintertime in Beijing, China, *Atmos. Chem. Phys.*, 13, 4577–4592, 2013.

Shaiganfar, R., Beirle, S., Sharma, M., Chauhan, A., Singh, R. P., and Wagner, T.: Estimation of NO_x emissions from Delhi using Car MAX-DOAS observations and comparison with OMI satellite data, *Atmos. Chem. Phys.*, 11, 10871–10887, doi:10.5194/acp-11-10871-2011, 2011.

Shaiganfar¹, R., Beirle, S., Petetin, H., Zhang, Q., Beekmann, M., and Wagner, T.: New concepts for the comparison of tropospheric NO₂ column densities derived from car-MAX-DOAS observations, OMI satellite observations and the regional model CHIMERE during two MEGAPOLI campaigns in Paris 2009/10, *Atmos. Meas. Tech.*, 8, 2827–2852, 2015.

Thalman, R. and Volkamer, R.: Temperature dependent absorption cross-sections of O₂-O₂ collision pairs between 340 and 630 nm and at atmospherically relevant pressure., *Phys. Chem. Chem. Phys.*, 15, 15371–15381, <https://doi.org/10.1039/c3cp50968k>, 2013.

van Donkelaar, A., Martin, R.V., Brauer, M., Kahn, R., Levy, R., Verduzco, C., Villeneuve, P.J. Global estimates of ambient Fine particulate matter concentrations from satellite-based aerosol optical depth: development and application. *Environ. Health Perspect.* 118, 847-855, 2010.

Vandaele, A. C., Hermans, C., Simon, P. C., Roozendael, M. V., Guilmot, J. M., Carleer, M., and Colin, R.: Fourier Transform Measurement of NO₂ Absorption Cross-Section in the Visible Range at Room Temperature, *J. Atmos. Chem.*, 25, 289–305, 1996.

Wang, Y. S., Yao, L., Wang, L. L., Liu, Z. R., Ji, D. S., Tang, G. Q., Zhang, J. K., Sun, Y., Hu, B., Xin, J. Y.: Mechanism for the formation of the January 2013 heavy haze pollution episode over central and eastern China. *Science China: Earth Sciences*, 57: 14–25, doi: 10.1007/s11430-013-4773-4, 2014a.

Wang, Z. F., Li, J., Wang, Z., Yang, W. Y., Tang, X., Ge, B. Z., Yan, P. Z., Zhu, L. L., Chen, X. S., Chen, H. S., Wang, W., Li, J. J., Liu, B., Wang, X. Y., Wang, W., Zhao, Y. L., Lu, N., Su, D. B.: Modeling

- study of regional severe hazes over mid-eastern China in January 2013 and its implications on pollution prevention and control, *Science China: Earth Sciences*, 57: 3–13, doi: 10.1007/s11430-013-4793-0, 2014b.
- 5 Wu, F. C., Xie, P. H., Li, A., Chan, K. L., Hartl, A., Wang, Y., Si, F. Q., Zeng, Y., Qin, M., Xu, J., Liu, J. G., Liu, W. Q., and Wenig, M.: Observations of SO₂ and NO₂ by mobile DOAS in the Guangzhou eastern area during the Asian Games 2010, *Atmos. Meas. Tech.*, 6, 2277–2292, 2013.
- Wu, Q. Z., Wang, Z. F., Gbaguidi, A., Gao, C., Li, L. N., and Wang, W.: A numerical study of contributions to air pollution in Beijing during CAREBeijing-2006, *Atmos. Chem. Phys.*, 11, 5997–6011, 2011.
- 10 Wang, S., Zhou, B., Wang, Z., Yang, S., Hao, N., Valks, P., Trautmann, T., and Chen, L.: Remote sensing of NO₂ emission from the central urban area of Shanghai (China) using the mobile DOAS technique, *J. Geophys. Res.*, 117, D13305, doi:10.1029/2011JD016983, 2012.
- Wang, M., Zhu, T., Zhang, J. P., Zhang, Q. H., Lin, W. W., Li, Y., Wang, Z. F.: Using a mobile laboratory to characterize the distribution and transport of sulfur dioxide in and around Beijing, *Atmos. Chem. Phys.*, 11, 11631–11645, 2011
- 15 Wang, M., Zhu, T., Zheng, J., Zhang, R. Y., Zhang, S. Q., Xie, X. X., Han, Y. Q., and Li, Y.: Use of a mobile laboratory to evaluate changes in on-road air pollutants during the Beijing 2008 Summer Olympics, *Atmos. Chem. Phys.*, 9, 8247–8263, 2009
- Wenig, M. O., Cede, A. M., Bucsela, E. J., Celarier, E. A., Boersma, K. F., Veefkind, J. P., Brinksma, E. J., Gleason, J. F., and Herman, J. R.: Validation of OMI tropospheric NO₂ column densities using direct-sun mode Brewer measurements at NASA Goddard Space Flight Center, *J. Geophys. Res.*, 20 133, D16S45, doi:10.1029/2007JD008988, 2008.
- World Health Organization: WHO Air quality guidelines for particulate matter, ozone, nitrogen dioxide and sulfur dioxide Global update 2005 summary of risk assessment, Geneva, Switzerland, 2006.
- 25 Xu, J., Ma, J. Z., Zhang, X. L., Xu, X. B., Xu, X. F., Lin, W. L., Wang, Y., Meng, W., and Ma, Z. Q.: Measurements of ozone and its precursors in Beijing during summertime: impact of urban plumes on ozone pollution in downwind rural areas, *Atmos. Chem. Phys.*, 11, 12241–12252, 2011.
- Xu, X. P., Wang, L. H., and Niu, T. H.: Air pollution and its health effects in Beijing, *Ecosyst. Health*, 4, 199–209, 1998.
- 30 Ying Qi, Wu Li, Zhang Hongliang: Local and inter-regional contributions to PM_{2.5} nitrate and sulfate

- in China, *Atmos. Environ.*, 94, 582-592, 2014
- Yang, F., Tan, J., Zhao, Q., Du, Z., He, K., Ma, Y., Duan, F., Chen, G., and Zhao, Q.: Characteristics of PM_{2.5} speciation in representative megacities and across China, *Atmos. Chem. Phys.*, 11, 5207–5219, 2011
- 5 Zhang, W., Zhu, T., Yang, W., Bai, Z., Sun, Y. L., Xu, Y., Yin, B., and Zhao, X.: Airborne measurements of gas and particle pollutants during CAREBeijing-2008, *Atmos. Chem. Phys.*, 14, 301–316, 2014
- Zhao, B., Wang, S. X., Wang, J. D., Fu, J. S., Liu, T. H., Xu, J. Y., Fu, X., Hao, J.: Impact of national NO_x and SO₂ control policies on particulate matter pollution in China, *Atmos. Environ.*, 77, 453-463, 2013a
- 10 Zhao, X. J., Zhao, P. S., Xu, J., Meng, W., Pu, W. W., Dong, F., He, D., and Shi, Q. F.: Analysis of a winter regional haze event and its formation mechanism in the North China Plain, *Atmos. Chem. Phys.*, 13, 5685–5696, 2013b
- Zhang, R., Jing, J., Tao, J., Hsu, S. C., Wang, G., Cao, J., Lee, C. S. L., Zhu, L., Chen, Z., Zhao, Y., and Shen, Z.: Chemical characterization and source apportionment of PM_{2.5} in Beijing: seasonal
- 15 perspective, *Atmos. Chem. Phys.*, 13, 7053–7074, 2013

Table 1 Summary of monitoring information of mobile DOAS. Wind data from airport meteorological data

<http://www.wunderground.com>. The wind data indicates the wind field at the time of mobile DOAS measurement.

Cycles	Date	Time(LT)	Routes	Wind Direction	Wind Speed (m/s)
Cycle 1	11 June	10:14-14:00	BJ-SJZ	BJ: southeast SJZ: southwest	BJ: 2~3 SJZ: 1~2
	12 June	10:24-14:05	SJZ-DZ	SJZ: southwest DZ: southwest	SJZ: 1~2 DZ: 3~4
	13 June	10:20-15:04	DZ-BD-CZ	DZ: southwest BD: south CZ: southwest	DZ: 4~5 BD: 2~3 CZ: 4~5
	14 June	10:02-13:45	CZ-ZZ	CZ: southwest ZZ: southwest	CZ: 4~5 ZZ: 4~5
	15 June	09:57-14:06	ZZ-BJ	ZZ: south BJ: south	ZZ: 2~3 BJ: 2
	Cycle 2	17 June	10:36-14:19	BJ-SJZ	BJ: northeast SJZ: northeast
18 June		10:02-13:32	SJZ-DZ	SJZ: north DZ: north	SJZ: 1~2 DZ: 1~2
20 June		10:25-15:05	DZ-BD-CZ	DZ: northwest BD: northwest CZ: northeast	DZ: 2~3 BD: 2~3 CZ: 3~4
21 June		09:57-13:24	CZ-ZZ	CZ: west ZZ: southwest	CZ: 3~4 ZZ: 2~3
Cycle 3		24 June	10:47-14:06	BJ-SJZ	BJ: southeast SJZ: south
	25 June	10:10-14:17	SJZ-DZ	SJZ: south DZ: south	SJZ: 1~2 DZ: 3~4
	26 June	09:43-14:01	DZ-BJ	DZ: southwest BJ: south	DZ: 4~5 BJ: 3~4
Cycle 4	2 July	10:24-14:13	BJ-SJZ	BJ: northwest SJZ: northwest	BJ: 5~6 SJZ: 3~4
	3 July	10:26-14:01	SJZ-DZ	SJZ: southwest DZ: southwest	SJZ: 2 DZ: 3~4
	4 July	10:12-11:54	DZ-CZ	DZ: southwest CZ: southeast	DZ: 3~4 CZ: 1~2
	5 July	09:55-13:40	CZ-BD-CZ	CZ: northeast BD: northeast	CZ: 3~4 BD: 3~4
	6 July	09:56-14:23	CZ-ZZ	CZ: southeast ZZ: southwest	CZ: 2~3 ZZ: 2~3
	7 July	10:12-13:21	ZZ-BJ	ZZ: southeast BJ: southeast	ZZ: 2~3 BJ: 2~3

Table 2 DOAS fit settings for the retrieval of SO₂ and NO₂.

Parameter	SO ₂ fitting	NO ₂ fitting
Fitting window	310-324 nm	338-370 nm
Polynomial degree	4	5
Intensity offset	Constant	Constant
SO ₂	293 K(Bogumil et al., 2003)	-
NO ₂	298 K(Vandaele et al., 1996)	298 K & 220 K (Vandaele et al., 1996)
HCHO	297 K (Meller and Moortgat, 2000)	297 K (Meller and Moortgat, 2000)
O ₃	293 K(Bogumil et al., 2003)	223 K & 243 K (Bogumil et al., 2003)
O ₄	-	293 K (Thalman and Volkamer, 2013)
Ring	Calculation from FRS with DOASIS	Calculation from FRS with DOASIS

Table 3 Both results measured through mobile DOAS and in-situ instruments along the southwest and southeast routes for different wind fields.

VCD [molec./cm ²]		South Wind	North Wind	Ratio	Average
Southwest Route	SO ₂	6.09×10 ¹⁶	2.35×10 ¹⁶	2.69	4.22×10 ¹⁶
	NO ₂	2.16×10 ¹⁶	1.22×10 ¹⁶	1.77	1.69×10 ¹⁶
Southeast Route	SO ₂	3.29×10 ¹⁶	3.51×10 ¹⁶	0.94	3.40×10 ¹⁶
	NO ₂	1.34×10 ¹⁶	9.68×10 ¹⁵	1.38	1.15×10 ¹⁶

5

Near surface Concentration [ppb]		South Wind	North Wind	Ratio	Average
Southwest Route	SO ₂	10.78	8.69	1.24	9.74
	NO ₂	130.55	92	1.42	111.28
Southeast Route	SO ₂	23.29	11.24	2.07	17.27
	NO ₂	119.12	116.82	1.02	117.97

*Ratio: defined as the value under southerly wind/northerly wind

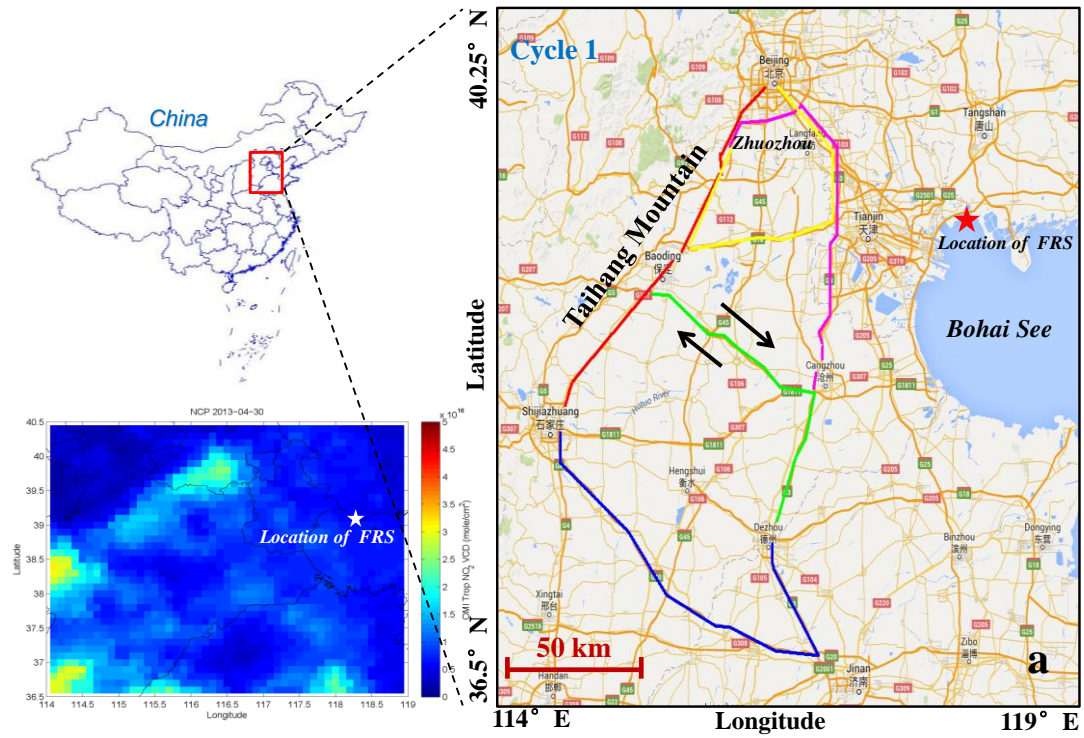


Figure 1: Maps of the mobile measurement areas and routes. The red, blue, green, pink, and yellow tracks show the routes of BJ–SJZ, SJZ–DZ, DZ–BD–CZ, CZ–ZZ, and ZZ–BJ (a). The OMI NO₂ VCD on 30 April shows the NO₂ VCD of FRS is low (a). (a) also marks the location of FRS, Bohai See, and Taihang Mountain. The red, blue, green, and pink tracks indicate the routes of BJ–SJZ, SJZ–DZ, DZ–BD–CZ, and CZ–ZZ (b). The red, blue, and yellow tracks show the routes of BJ–SJZ, SJZ–DZ, and DZ–BJ (c). The red, blue, green, pink, yellow, and black tracks show the routes of BJ–SJZ, SJZ–DZ, DZ–CZ, CZ–BD–CZ, CZ–ZZ, and ZZ–BJ (d). The black arrows indicate the monitoring route from CZ to BD and return to CZ.

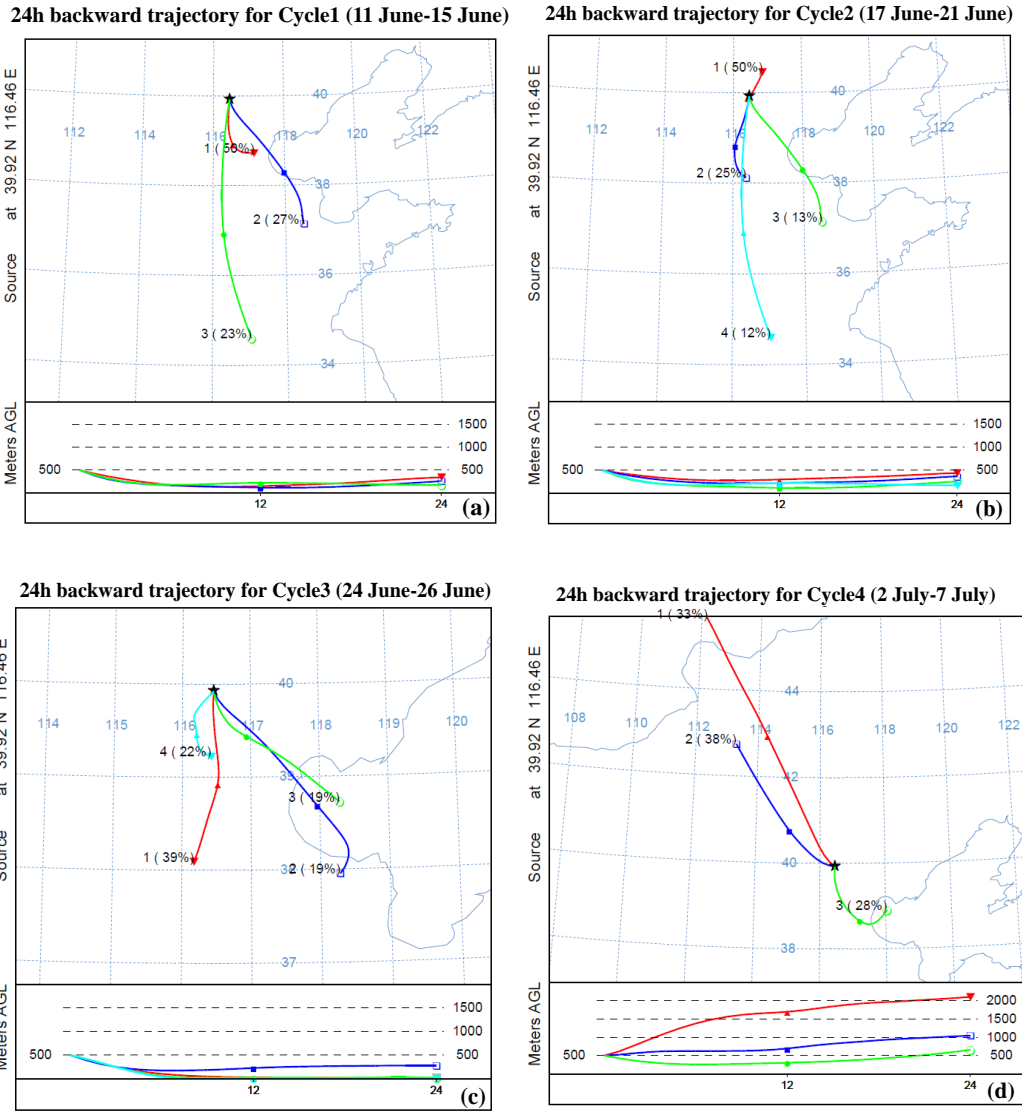


Figure 2: 24 h cluster mean air mass backward trajectories at 500 m height at Beijing for four different cycles. The black star shows the location of Beijing. The different color lines indicate air mass from different regions. (a), (b), (c), and (d) show the backward trajectory for Cycles 1, 2, 3, and 4, respectively. The percentages suggest the ratios of air mass in one region.

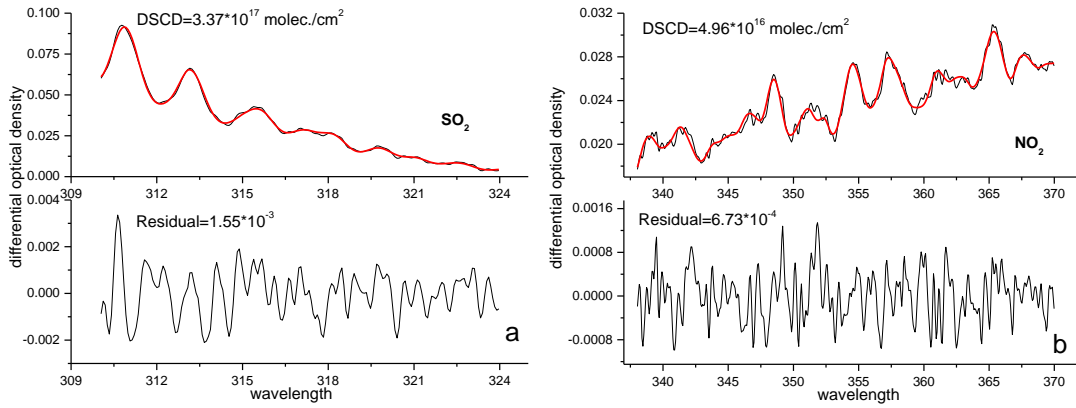


Figure 3: Example of SO₂ (a) and NO₂ (b) DSCD fit recorded at 13:04 (LT) on 12 June 2013. Black lines denote the differential optical densities (DODs) of measured spectrum, and red lines show the fit results. The DSCD is the SCD (Slant Column Density) with respect to FRS spectrum.

5

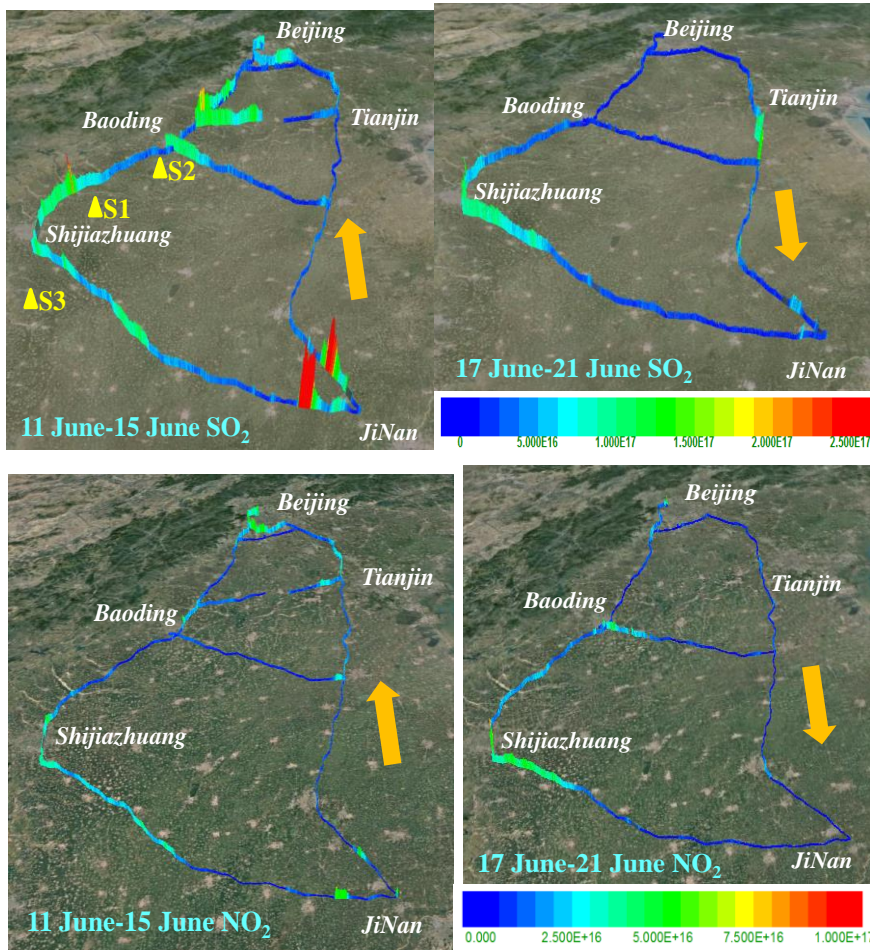


Figure 4: Spatial distributions of SO₂ and NO₂ VCDs over NCP area for north (17–21 June) and south (11–15 June) wind fields; the orange arrows show the dominant wind direction; the yellow triangles show three different locations of main SO₂ sources in the southwest of measurement region.

10

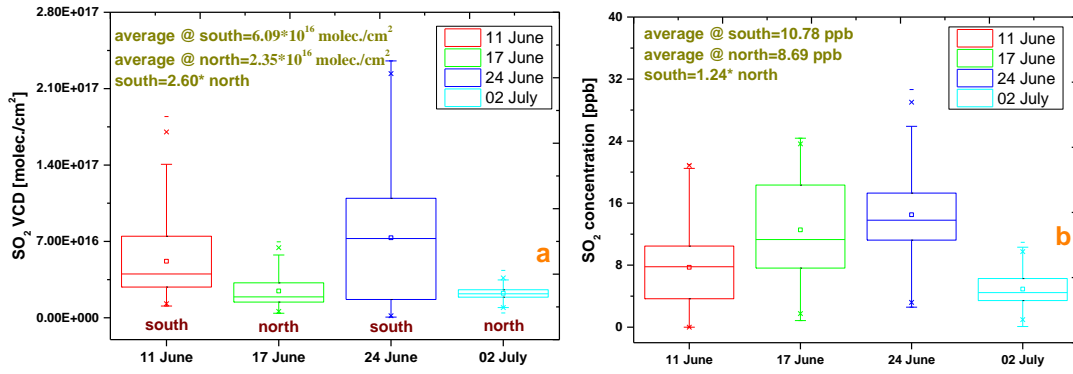
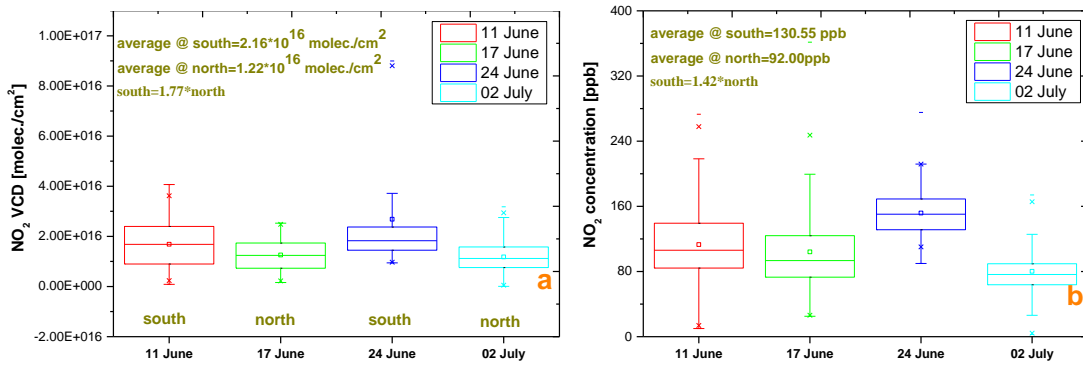


Figure 5: The SO₂ VCDs (a) and near-surface concentrations (b) along the southwest route.



5

Figure 6: The NO₂ VCDs (a) and near-surface concentrations (b) along the southwest route.

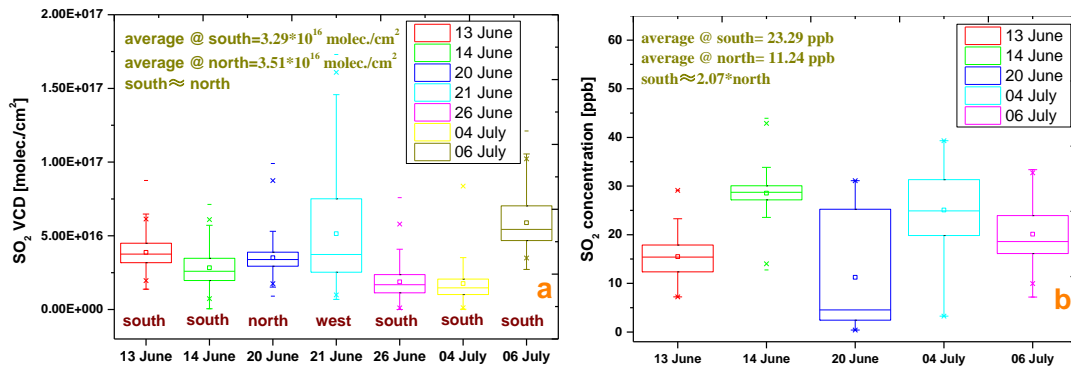


Figure 7: The SO₂ VCDs (a) and near-surface concentrations (b) along the southeast route; lack of near-surface data on 21 June and 26 June due to instrument problems.

10

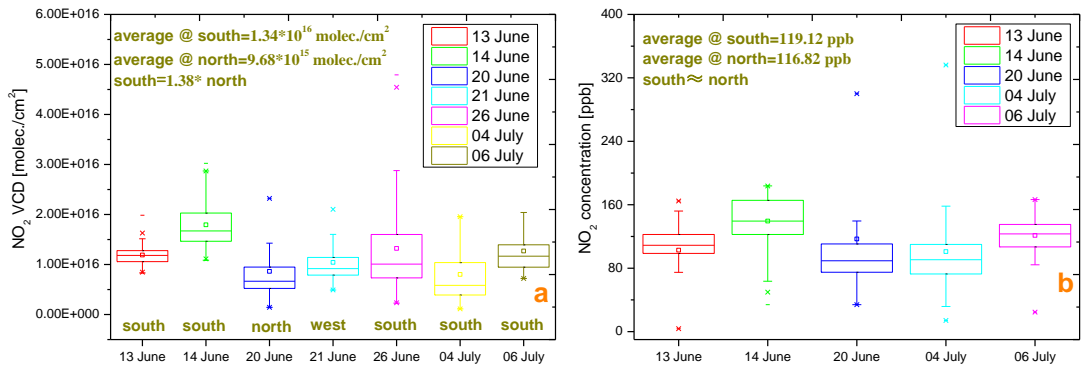


Figure 8: The NO₂ VCDs (a) and near-surface concentrations (b) along the southeast route; lack of near-surface data on 21 June and 26 June due to instrument problems.

5

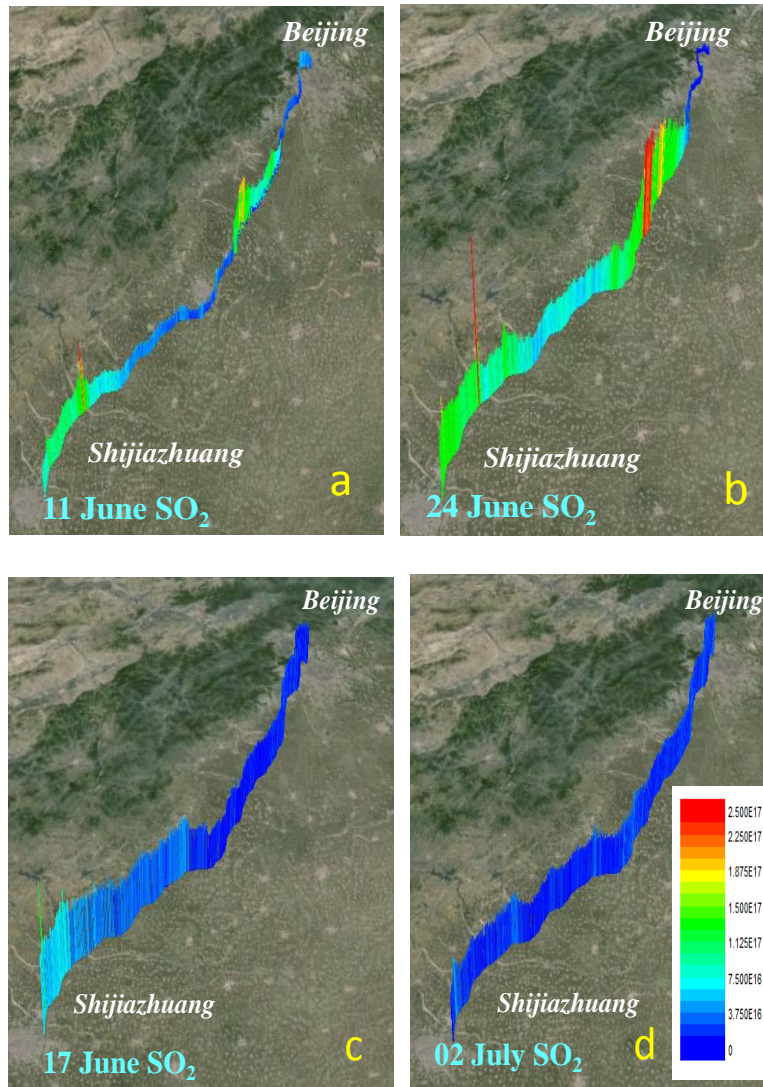


Figure 9: The variations of SO₂ VCDs along the southwest measurement routes (Beijing–Shijiazhuang) for south (a and b) and north (c and d) wind fields.

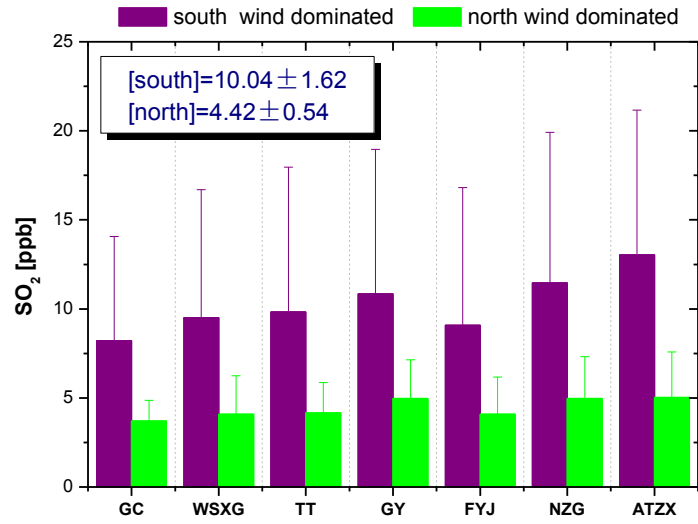
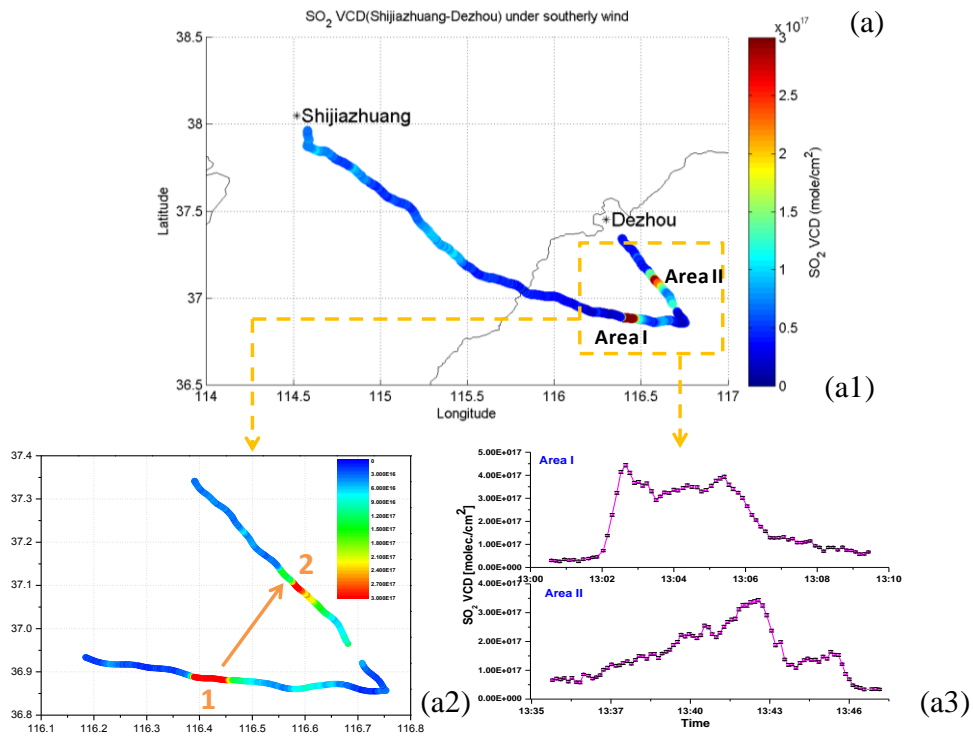


Figure 10: The mean concentrations of SO₂ measured at Gucheng (GC), Wanshou Xigong (GSXG), Tian Tan (TT), Guangyuan (GY), Fuyoujie (FYJ), Nongzhanguan (NZG), and AoTiZhongxin (ATZX) sites based on the south wind and north wind dominance in Beijing during mobile DOAS observations period. The bars show the standard deviations of SO₂ concentrations.

5



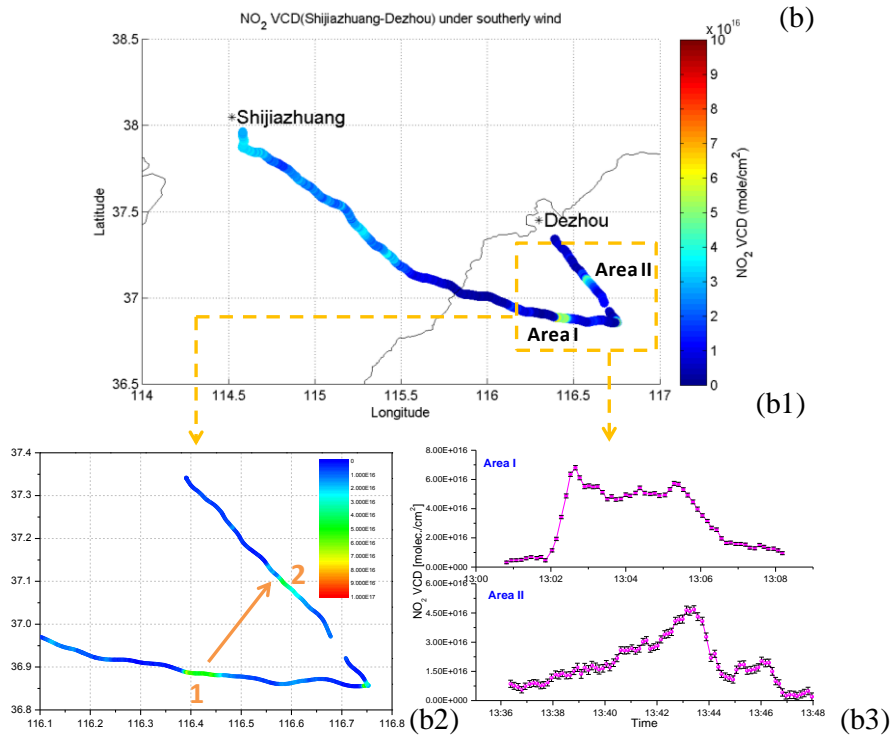
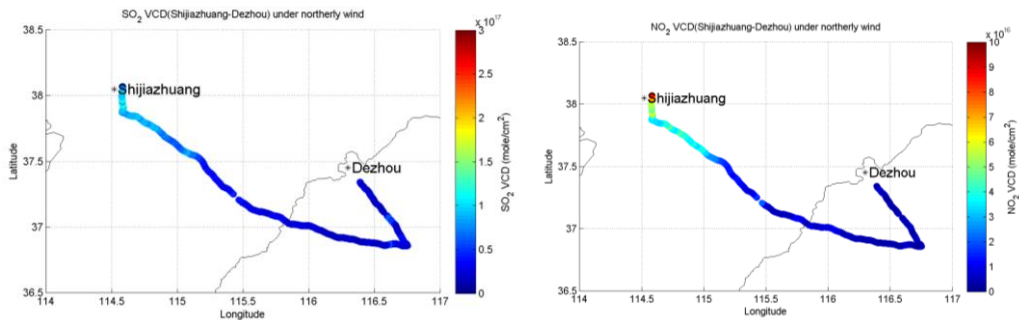


Figure 11: The hot spots of SO₂ (a) and NO₂ VCDs (b) are observed for the measurement of Shijiazhuang–Dezhou city under southerly wind on 12 June. (a1): Distribution of SO₂ VCDs along the whole measurement route; (a2) Distribution of SO₂ VCDs on hot spot area, where the origin arrow shows the diffusion of air mass from location 1 to location 2; (a3) time series of SO₂ VCDs for the polluted air mass for the rectangular area as shown in (a1), where the top figure of (a3) shows the Area I and the bottom for the Area II. (b1), (b2), and (b3) are similar as (a1), (a2), and (a3), only for NO₂.



10 Figure 12: The distributions of SO₂ and NO₂ VCDs along the Shijiazhuang–Dezhou measurement route for northerly wind on 18 June.

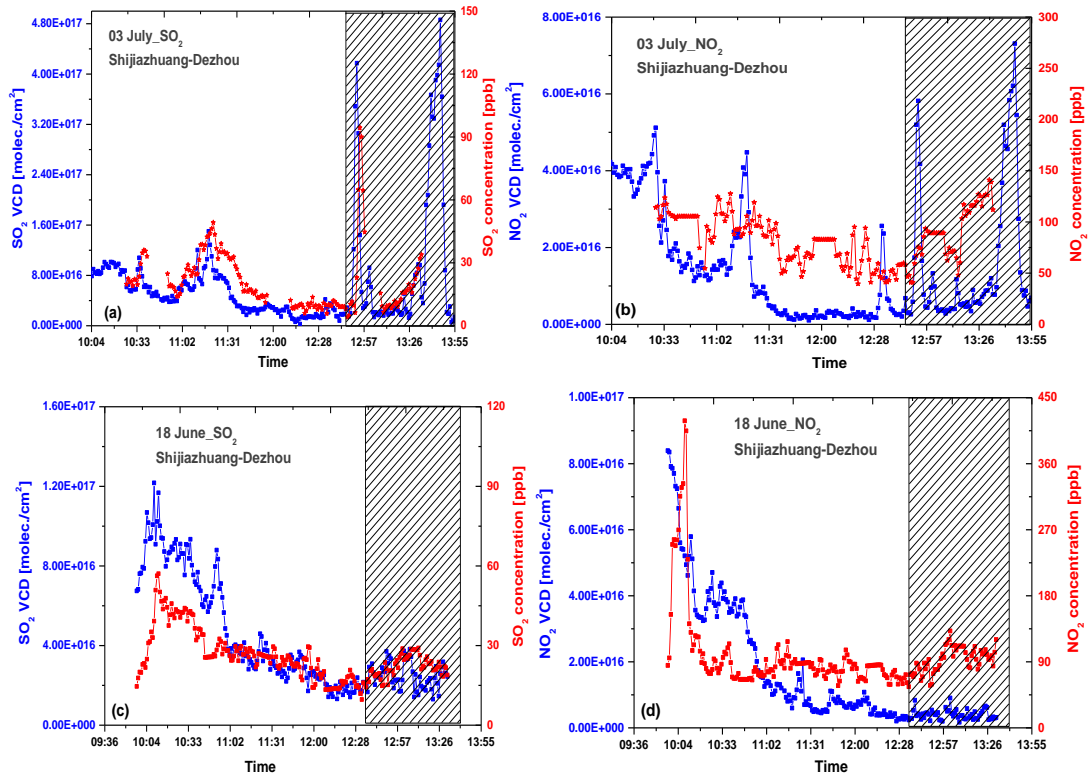


Figure 13: Time series of VCDs and near-surface concentrations of SO₂ and NO₂ along the route of Shijiazhuang-Dezhou for south and north wind. (a) and (b): SO₂ and NO₂ VCDs and near-surface concentrations on 3 July under southerly wind; (c) and (d): SO₂ and NO₂ VCDs and near-surface concentrations on 18 June under northerly wind;

The sparse rectangular boxes show polluted air mass area as shown in Fig. 11.

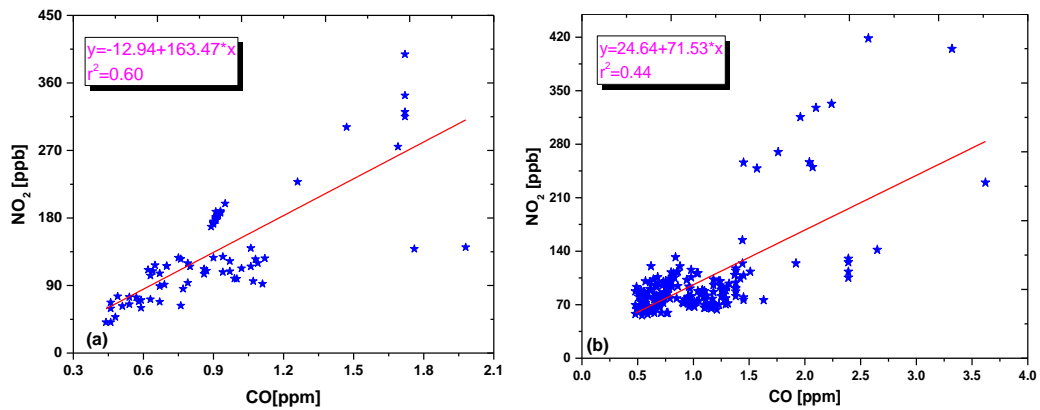
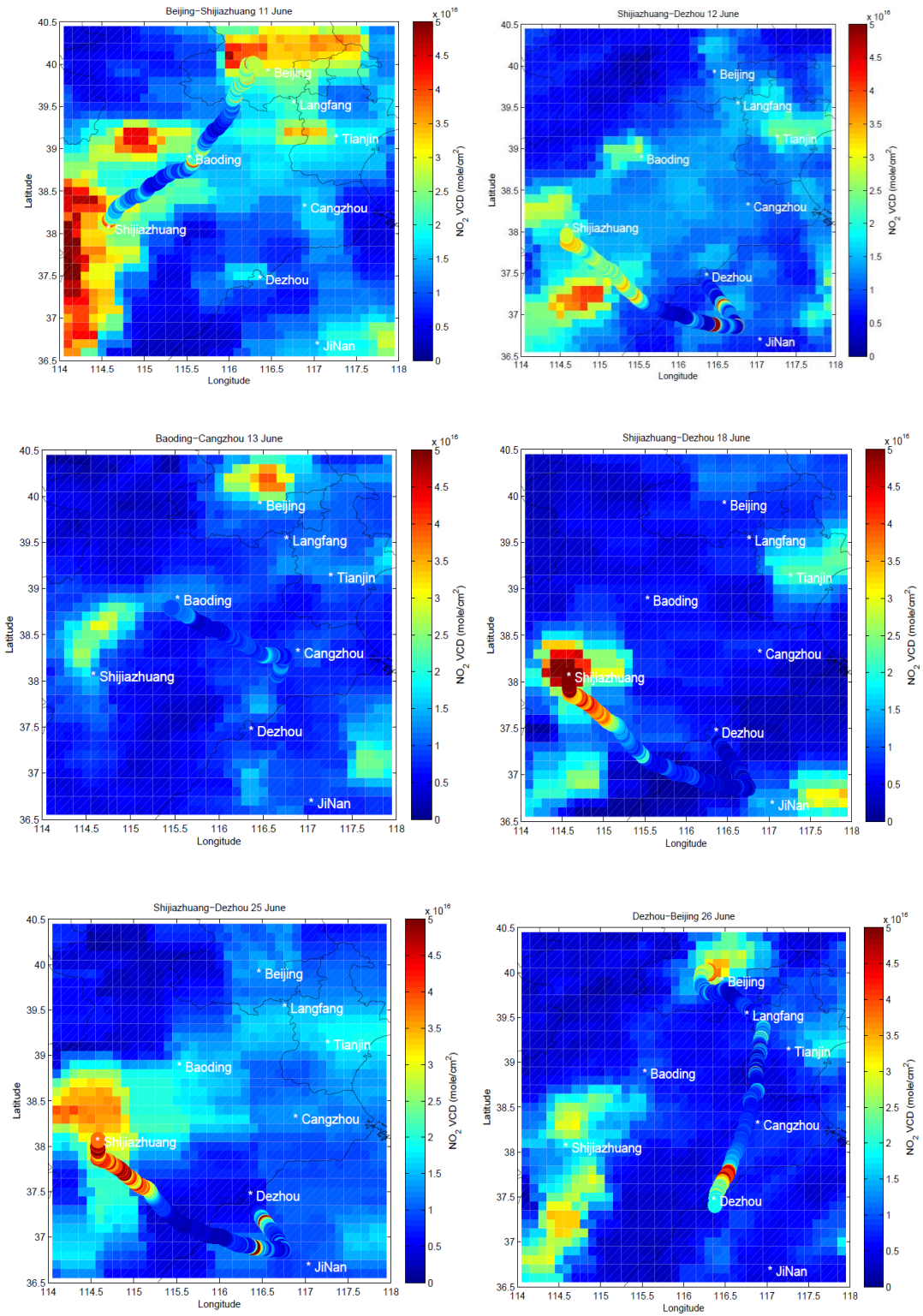


Figure 14: Correlation analysis between NO₂ and CO near-surface concentrations for the sparse rectangle area as

shown in Fig. 13; (a): south wind; (b) north wind.



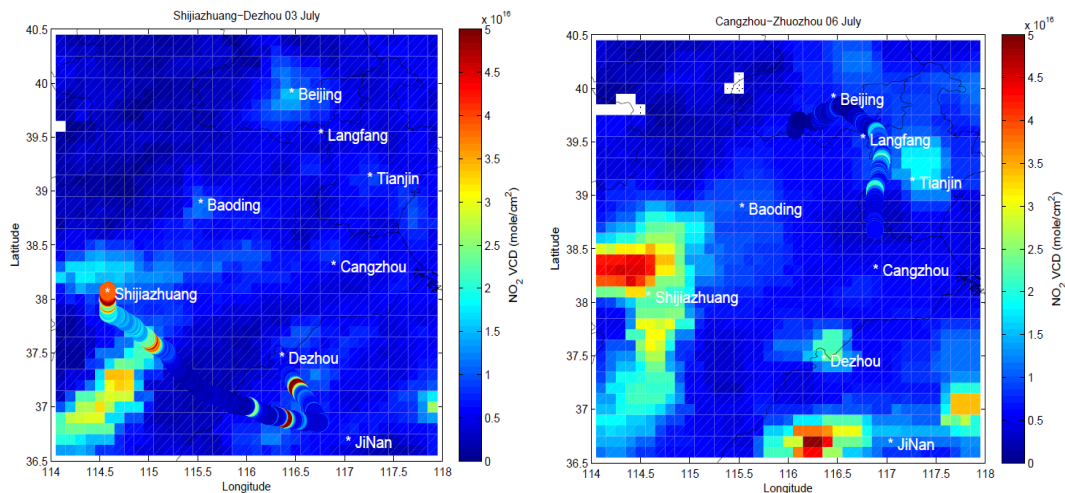


Figure 15: Spatial pattern of NO_2 measured through mobile DOAS and OMI. The header of each plot indicates measured route and date, such as the first plot showing the result of “Beijing–Shijiazhuang” route on 11 June. The color-coded circle indicates the mobile DOAS observations. The grid resolution of OMI was $0.1^\circ \times 0.1^\circ$.

5

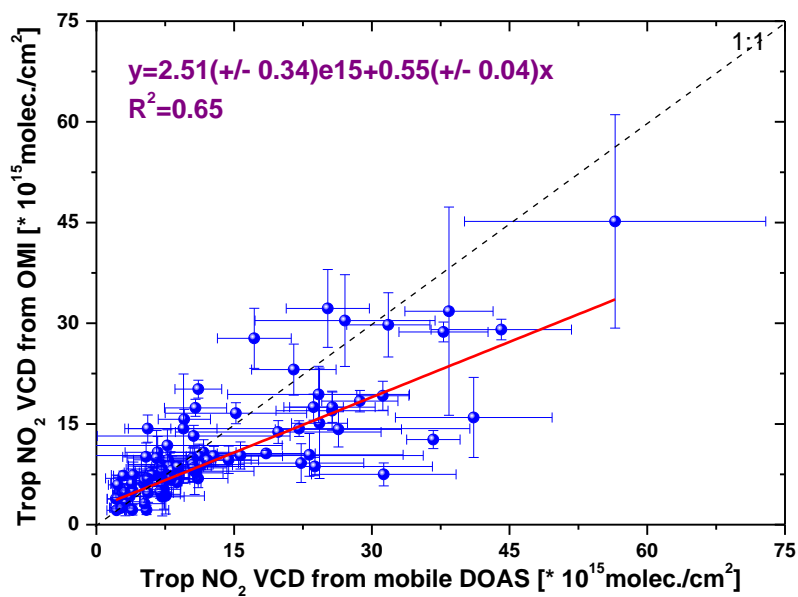


Figure 16: Correlation analysis of mobile DOAS and OMI NO_2 VCDs. The error bars show the OMI error and standard deviation of mobile DOAS as described in the text.